

# Advanced Epitaxial Lift-Off and Transfer Procedure for the Fabrication of High-Quality Functional Oxide Membranes

Jordan Bouaziz,<sup>\*</sup> Claudia Cancellieri, Bastian Rheingans, Lars P. H. Jeurgens, and Fabio La Mattina<sup>\*</sup>

In the past 5 years, the transfer of epitaxial oxide thin films has drawn a renewed interest in the scientific community. The major challenge in this technology is to minimize the appearance of extended bulk defects such as plastic deformations, cracks, and delamination, which are induced by the transfer process to a new host substrate. In this work, a procedure for the transfer of epitaxial oxide films where a rigid bond to the final host holder is obtained via a metallic Au/Ag bonding layer is presented. Here, the transfer of SrRuO<sub>3</sub> (SRO) and SrRuO<sub>3</sub>/SrTiO<sub>3</sub> (STO) epitaxial films grown on a water-soluble Sr<sub>3</sub>Al<sub>2</sub>O<sub>6</sub> sacrificial layer is reported. These epitaxial films are grown on a STO substrate and transferred onto a Si host substrate. Roughness values lower than 1 nm are observed for the transferred SRO membranes. Cross-section analysis shows straight interfaces without plastic deformation of the membranes. X-ray diffraction rocking-curve analysis evidences that mechanical damage is minimized and the membranes remain close to their initial quality. This procedure represents an important step forward in the development of advanced technologies for membrane transfer of epitaxial oxides and superstructures.

In the III–V materials sector, various so-called “epitaxial lift-off” procedures have been developed over the last 30 years.<sup>[11,12]</sup> The currently employed transfer methods for perovskite oxide membranes are very similar to these previously developed “epitaxial lift-off” procedures. The earliest proposed procedures for perovskite oxides are based on acid etching,<sup>[13–15]</sup> thermal melting (laser lift-off),<sup>[16]</sup> and layer splitting by helium and/or hydrogen implantation.<sup>[17]</sup> These methods generally preserve the single-crystal nature of the films after the transfer. However, most of these technologies can only be used for a limited number of materials.

The more recently developed lift-off method by Lu et al.<sup>[18]</sup> relies on the fabrication of a water-soluble Sr<sub>3</sub>Al<sub>2</sub>O<sub>6</sub> (SAO) sacrificial interlayer between the parent substrate and the epitaxial thin-film membrane; it can thus be exploited for all membrane materials which are chemically inert to water. Importantly, SAO can be

## 1. Introduction

Perovskite oxides are intensively investigated for their enormous variety of physical properties and for their potential as next-generation electronic materials. Their property range includes high temperature superconductivity, piezoelectricity, ferroelectricity, ferromagnetism, multiferroic behavior, resistive switching behavior, ionic conduction, and catalytic properties.<sup>[1,2]</sup> The epitaxial synthesis of these complex metal oxide thin films typically involves high temperature<sup>[3]</sup> and specific substrate requirements for epitaxial growth.<sup>[4–7]</sup> Unfortunately, these requirements are in most cases not compatible with industrial processes such as back-end-of-line integration<sup>[8]</sup> in CMOS industry.<sup>[9,10]</sup>

grown epitaxially on SrTiO<sub>3</sub> (STO), which is one of the most frequently used parent substrates for epitaxial thin film growth, and in the past few years, it has therefore been extensively used as a sacrificial layer for epitaxial transfer of oxide membranes.<sup>[19–24]</sup> Generally, this compound is deposited by pulsed laser deposition (PLD),<sup>[18,21,25–28]</sup> but few authors already tried to synthesize it by molecular beam epitaxy,<sup>[22,29]</sup> chemical solution deposition,<sup>[30]</sup> and radio-frequency magnetron sputtering.<sup>[31]</sup> By exploiting SAO as a sacrificial layer, a wide variety of oxides (and their heterostructures), mostly perovskites,<sup>[18,22,25,32–34]</sup> but also binary oxides,<sup>[30,35–37]</sup> have been successively transferred from the parent STO substrate onto other host substrates. Other parent substrates such as LaAlO<sub>3</sub>,<sup>[31]</sup> Al<sub>2</sub>O<sub>3</sub>,<sup>[37]</sup> and MgO<sup>[38]</sup> have also been used as seed crystal for epitaxial growth of SAO.

Before dissolving the sacrificial SAO layer in water, any functional overlayers on top (further designated as *membrane*) need to be coated with an adhesive for subsequent attachment to the host substrate. Polydimethylsiloxane (PDMS) adhesive has been extensively used,<sup>[18,20,22,25,39]</sup> but it is sometimes replaced by photoresists,<sup>[27,33,36]</sup> tapes (polyimide tapes like Kapton or thermal release tapes),<sup>[29,34,36]</sup> or epoxy glue.<sup>[40]</sup> Membrane transfer strategies without the use of adhesives also exist, like the so-called “fishing” method,<sup>[31,37,41]</sup> or the more recently developed procedure by Sambri et al. which does not use any sacrificial layer.<sup>[42]</sup>

Most membrane lift-off and transfer methods used up to date have been at least partially inspired by the developed

J. Bouaziz, C. Cancellieri, B. Rheingans, L. P. H. Jeurgens, F. La Mattina  
Empa  
Swiss Federal Laboratories for Materials Science and Technology  
Überlandstrasse 129, Dübendorf CH-8600, Switzerland  
E-mail: jordan.bouaziz@empa.ch; fabio.lamattina@empa.ch

The ORCID identification number(s) for the author(s) of this article can be found under <https://doi.org/10.1002/admi.202201458>.

© 2022 The Authors. Advanced Materials Interfaces published by Wiley-VCH GmbH. This is an open access article under the terms of the Creative Commons Attribution License, which permits use, distribution and reproduction in any medium, provided the original work is properly cited.

DOI: 10.1002/admi.202201458

transfer procedures for graphene sheets (and other 2D materials such as hBN<sup>[43]</sup>). For instance, the exfoliation<sup>[44]</sup> and the “fishing” methods<sup>[45]</sup> are commonly applied for the transfer of graphene sheets, since graphene shows a very strong resistance to stress-induced damage;<sup>[46]</sup> this eases handling and, more importantly, prevents unwanted defect formation during transfer. On the contrary, freestanding perovskite oxide thin films are very brittle. They are easily deformed by the acting forces originating from the surface tension of contacting water. Indeed, oxide membranes transferred with the help of a sacrificial water-soluble layer generally contain defects, cracks, and plastic deformations (delamination and wrinkles).<sup>[18,47,48]</sup> Several competing phenomena are held responsible for the formation of these defects: the interaction between thin film and water (surface tension), strain relaxation in the epitaxial membrane upon detachment, as well as bad adhesion of the transferred membrane with the host substrate.

In this article, a new transfer method is proposed in which membranes of SrRuO<sub>3</sub> (SRO) and SRO/STO are directly transferred to the host substrate, with no need of intermediate mechanical support. To this end, prior to the SAO layer water-dissolution step, a solid metallic joint is created between the membrane surface and the final host substrate by low-temperature sinter-bonding using Ag nanopaste. To assess the quality of the transferred membranes, their defect structures and surface morphologies were characterized before and after the transfer procedure by X-ray diffraction (XRD), light optical microscopy (LOM), scanning electron microscopy (SEM), and atomic force microscopy (AFM). The transferred SRO and SRO/STO membranes are found to be smooth and crack- and wrinkle-free across almost the entire transferred area (10–21 mm<sup>2</sup>) without any major modifications of their as-grown defect structures.

## 2. Results and Discussion

### 2.1. Transfer Method

As discussed in Section 1, the transfer of epitaxial (i.e., single-crystalline) oxide membranes from their parent substrate onto a different host substrate is highly challenging. To prevent any deformation and/or relaxation of the oxide membrane during its detachment from the parent substrate, the fragile oxide membrane should be gently, but firmly bonded to the host substrate prior to the water dissolution step. However, soft and rather flexible adhesive materials, such as PDMS, photoresists, PI-tape, or epoxy glue, are commonly used to “stick” the oxide membrane to the host substrate by relatively weak adhesive forces. Chemical bonding of the oxide membrane to the host substrate by a filler metal or alloy would create a more firm joint, thereby strengthening the membrane structure during the lift-off procedure. Accordingly, in the following a novel transfer method for epitaxial oxide membranes is proposed, which incorporates a joining step by low-temperature sinter-bonding (using Ag-nanopaste) prior to the sacrificial SAO interlayer dissolution step, as schematically illustrated in **Figure 1**.

#### 2.1.1. Deposition

A sacrificial SAO layer with a typical thickness in the range of 20–40 nm was epitaxially grown on a TiO<sub>2</sub>-terminated (001)-oriented STO substrate (size 5 × 5 mm<sup>2</sup>) by PLD (step 1, Figure 1a): see Section 4. Next, a thin oxide film composed by SRO or STO/SRO heterostructure (with a variable thickness in the range of 20–120 nm) was epitaxially grown onto SAO in the

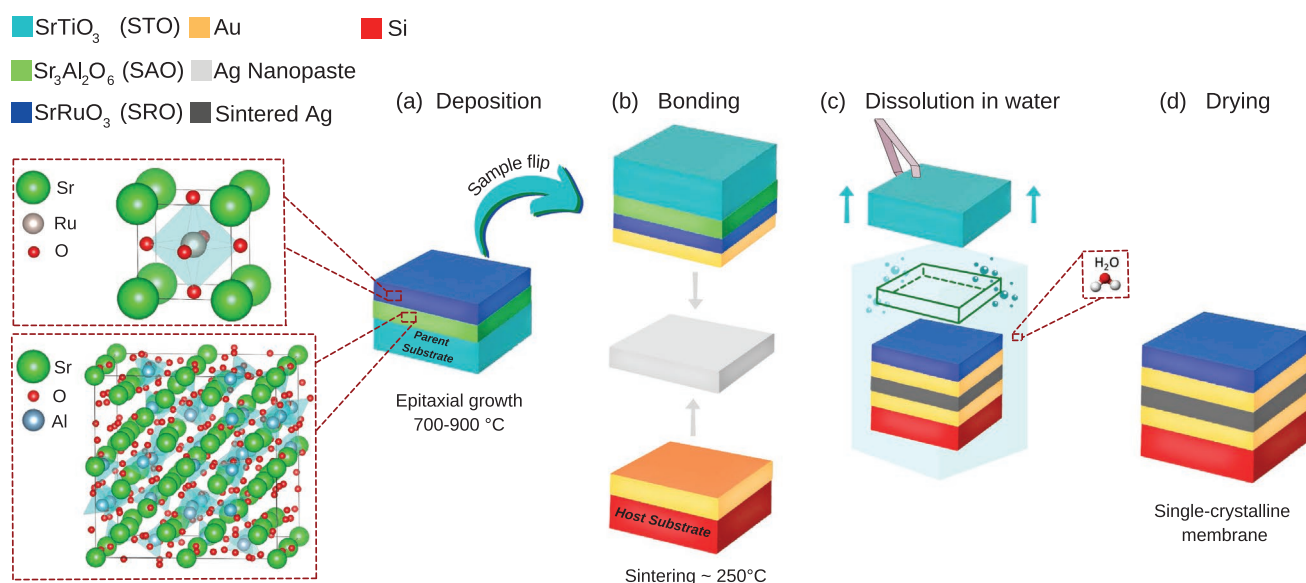


**Figure 1.** Schematic illustration of the subsequent steps for membrane manufacturing and transfer via silver nanopaste sinter-bonding. a) Deposition of a sacrificial SAO interlayer (20–40 nm) and SRO overlayer (20–120 nm) by PLD. b) Sputter-deposition of a 100 nm-thick Au metallization on the SRO overlayer and the Si host substrate, followed by stencil printing of the Ag nanopaste (20–50 μm). Next, the joint assembly was sintered at around 250 °C for 30 min. c) Dissolution of the SAO sacrificial layer in H<sub>2</sub>O and removal of the STO parent substrate. d) After drying, the final structure with, on top, the SRO single-crystalline membrane is obtained.

same PLD run. In this case study, SRO was selected as oxide membrane material, since it is an archetype of functional oxide which grows epitaxially on both STO<sup>[49]</sup> and SAO.<sup>[50]</sup>

### 2.1.2. Bonding

Next, the surfaces of the oxide membrane and the host substrates (here Si) were prepared for Ag bonding by sputter-deposition of a 100-nm-thick Au metallization layer on top (step 2, Figure 1b). Notably, the edges of oxide membranes were protected (covered) during the Au coating step in order to prevent Au deposition on the edges of the SRO/SAO stack. Au is commonly used as a metallization layer to facilitate bond formation with Ag. Moreover, the Au metallization acts as an inert buffer layer to prevent adverse reactions between the Ag nanopaste and the oxide membrane. Next, a commercial Ag nanopaste, consisting of Ag nanoparticles and organic additives (surfactants, binders, solvents), was applied either on the membrane or on the host substrate by stencil printing. Notably, the procedure for low-temperature sinter-bonding using commercially available Ag-paste is well-established and broadly-applied in electronics industry, for example, for die-attach on heat sinks.<sup>[51]</sup> Upon annealing in air at a relatively low temperatures (<300 °C), the organic components in the paste decompose and the Ag nanoparticles sinter, thereby forming a metallic sinter-bond with varying degree of porosity (depending on, e.g., the applied temperature and pressure).<sup>[51]</sup> The dominating thermodynamic driving force for this solid-state sintering process is the minimization of the surface energy of the Ag particles. In the present study, Ag nanopaste sinter-bonding was performed for 30 min at 250 °C on a flip-chip bonder, applying a controlled bonding force of 2 N: see Section 4 for more details. The bonding process can also be performed by manual assembly, followed by a sintering step in an air furnace (regulated in the temperature range between 250 and 260 °C) with a defined weight on top (further referred to as manual method).

Two different approaches for Ag-paste application were evaluated. First attempts were made by applying the Ag-paste manually on the surface of the Au-coated Si host substrate (i.e., without using stencil printing). Outflow of Ag paste on the edge of the as-grown heterostructure was prevented by choosing a smaller area of the host substrate (i.e.,  $3 \times 3 \text{ mm}^2$  and  $3 \times 7 \text{ mm}^2$ ) as compared to the as-grown oxide membrane (i.e.,  $5 \times 5 \text{ mm}^2$  and  $5 \times 10 \text{ mm}^2$ , respectively). However, these initial attempts did not allow the application of a defined and uniform thickness of the Ag paste for the subsequent sinter-bonding step, which resulted in a non-reproducible and unsatisfactory membrane transfer procedure. More reproducible results were obtained by applying a defined bond line thickness by stencil printing using 20  $\mu\text{m}$ -thick stainless steel masks with print areas between  $3 \times 3 \text{ mm}^2$  to  $5 \times 5 \text{ mm}^2$ .

### 2.1.3. Dissolution in Water

As shown in step 3, Figure 1c, after sinter-bonding, the joint assembly was placed in a beaker of milliQ-H<sub>2</sub>O to dissolve the sacrificial SAO interlayer. Notably, the dissolution process

is extremely fast (few minutes) if the entire SAO surface area is directly exposed to water (as tested in the present study; see also refs. [29, 52]). However, for the transfer method according to Figure 1, the dissolution of the sacrificial SAO interlayer in water will be significantly slower, since the dissolution proceeds in a crevice (i.e., confined) geometry and can thus only progressively proceed from the edges of the SAO layer. The solubility limit in such a crevice geometry will be reached within seconds. Continuous dissolution of the SAO interlayer then relies on the diffusion (exchange) rate(s) of dissolved ionic species from the inside to the outside of the crevice (similar to the exchange of ionic species during crevice corrosion). Dissolution tests performed in this study show that the dissolution of the SAO interlayer in an sufficiently large reservoir of deionized water (without stirring) was typically completed within 1 day. However, as discussed above, special attention should be paid to prevent the pressing-out of Ag paste at the stack edges during the sinter-bonding process, or coverage with Au metallization, since this will partially block the accessible area for water penetration. In such a case, the dissolution kinetics might be extremely slow and also an easy detachment of the membrane from the parent substrate may be hindered. To ensure complete and gentle detachment of the thin oxide membrane, the parent STO substrate was only removed after 4 days.

### 2.1.4. Drying

The final structure with the functional oxide membrane on top of the host substrate is obtained after drying (step 4, Figure 1d). As will be demonstrated in Sections 2.3 and 2.4, the proposed transfer method not only minimizes the mechanical stress exerted on the thin oxide membrane during the sacrificial SAO interlayer dissolution step, but also provides a firm mechanical contact between the transferred membrane and its host substrate, which is also electrically and thermally conducting.

## 2.2. XRD Characterization of Sacrificial Sr<sub>3</sub>Al<sub>2</sub>O<sub>6</sub> Layer

It is well established that SAO can grow epitaxially on top of (001)-oriented STO substrates.<sup>[18,53]</sup> Indeed, both phases have a cubic crystal structure and the lattice constant of SAO approximately matches four times the lattice constant of STO ( $a_{\text{SAO}} \approx 4 \times a_{\text{STO}}$ ). The epitaxial growth of this sacrificial layer was confirmed by XRD. To this end, 80-nm-thick SAO film was grown on STO by PLD (see Section 4) and subsequently capped with 20-nm-thick STO layer to prevent reaction with air humidity.<sup>[29]</sup> A schematic of the geometry of the XRD analysis is presented in the Supporting Information. As shown in Figure 2a, only (001)-diffraction peaks were detected by the XRD  $\theta$ -2 $\theta$  scan, confirming the expected (001) in-plane texture of the epitaxial SAO thin film.<sup>[54,55]</sup> In few cases, a slightly different diffraction pattern for SAO grown on (001)-oriented STO substrate has been reported; in particular, SAO (008) reflections were reported at angles as low as  $\approx 42.3^\circ$ , as attributed to a tetragonal highly strained SAO phase<sup>[33,56]</sup> of unclear origin. In the present work, a cubic SAO phase was obtained.<sup>[54,55]</sup> Rietveld refinement of the XRD diffractogram, as measured from the polycrystalline

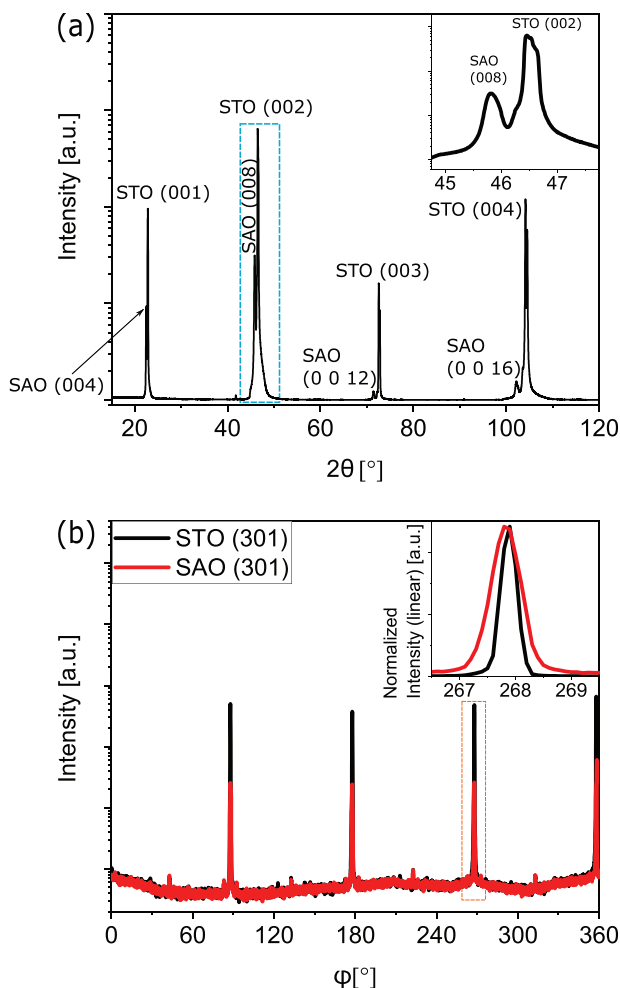


**Figure 2.** a,b) XRD scans of a 80 nm-thick  $\text{Sr}_3\text{Al}_2\text{O}_6$  thin film grown on a  $\text{SrTiO}_3$  substrate capped with 20 nm-thick  $\text{SrTiO}_3$  layer ( $\approx 20$  nm): a)  $\theta$ - $2\theta$  scan at  $\chi = 0^\circ$ , b)  $\phi$ -scans at  $2\theta = 77.20^\circ$  (black curve),  $2\theta = 75.91^\circ$  (red curve), and at  $\chi = 71.60^\circ$  (angle between (001) and (301) planes). Configuration set-up can be found in Figure S1, Supporting Information.

SAO deposition target, gives an unstrained lattice parameter for bulk (cubic) SAO of  $15.8392 \pm 0.0004$  Å, which is only marginally larger than four times the unstrained lattice parameter of STO (i.e.,  $4 \times a_{\text{STO}} = 15.620$  Å). Consequently, epitaxial growth of a thin SAO film on a STO substrate results in an in-plane compression and associated out-of-plane expansion of the SAO film, as experimentally confirmed from the corresponding derived out-of-plane ( $15.850 \pm 0.004$  Å) and in-plane ( $15.76 \pm 0.03$  Å) lattice parameters (see Supporting Information, for more details).

Further confirmation of crystallographic orientation of the film relative to the substrate was obtained by comparing  $\phi$ -scans of the SAO and STO (301)-reflection lines, as shown in Figure 2b. The film (red line) exhibits a fourfold symmetry with all the equivalent principal axes (cubic) aligned with the STO ones. The full width at half maximum (FWHM) of the SAO peaks (inset in Figure 2b) are broader than the substrate ones, which is consistent with the fact that the film contains some dislocations related to interface strain and possible bulk defects, as investigated in more detail in Section 2.3.

### 2.3. XRD Characterization of $\text{SrRuO}_3$ Films and Transferred Membranes

In Figure 3a, XRD  $\theta$ - $2\theta$  scans for a 85-nm-thick SRO membrane grown on a 40-nm-thick SAO layer on the STO substrate are presented before (“as-grown”) and after (“membrane”) transfer. Since the film and substrate reflection lines largely overlap, a  $\approx 85$  nm-thick SRO film was grown in order to be able to distinguish its diffraction peaks. Indeed, the (001)-reflections of the pseudo-cubic phase of SRO<sup>[57]</sup> can be distinguished at slightly lower  $2\theta$  angles than the corresponding STO peaks.<sup>[49]</sup> A zoom in the  $2\theta$  range from  $42^\circ$  to  $52^\circ$  is shown in Figure 3b. After the sinter-bonding and water dissolution steps, the SAO and STO substrate peaks have disappeared and only the (001)-reflections of SRO remain. X-ray photoemission (XPS) analysis of the surfaces of the transferred membrane reveals only a tiny residual trace of SAO lower than 1 at% (see Supporting Information), thus evidencing a successful and complete dissolution of the sacrificial layer. Notably, the SRO crystal lattice parameters

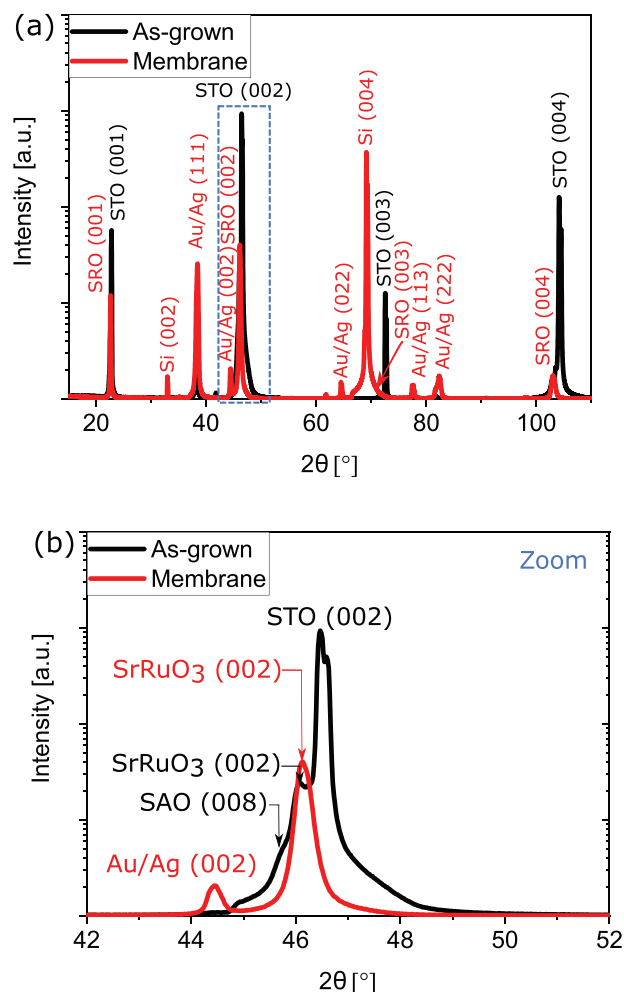


**Figure 3.** XRD scans: comparison between an as-grown  $\text{SrRuO}_3$  (85 nm)/ $\text{Sr}_3\text{Al}_2\text{O}_6$  (40 nm)/ $\text{SrTiO}_3$  sample (black curves) and a transferred  $\text{SrRuO}_3$  (85 nm) membrane (red curve): a)  $\theta$ - $2\theta$  scan at  $\chi = 0^\circ$ . b) Zoom on the most intense peaks from the oxide film pertaining the scan in (a). The peaks which are not labeled in (a), belong to the holder or to the non monochromatic radiation.



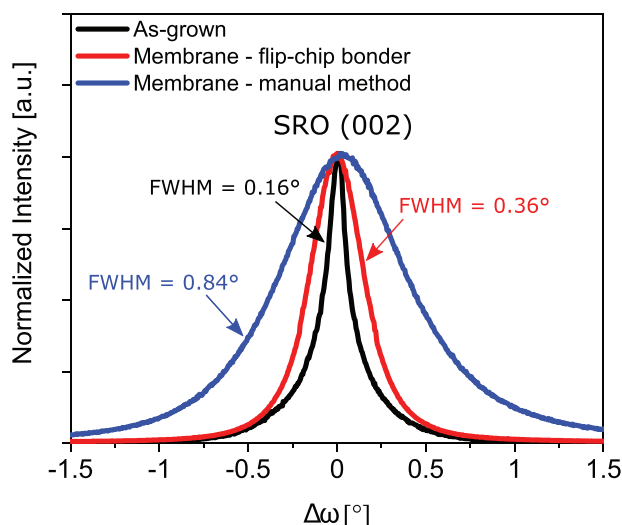


**Figure 4.** Rocking-curve of the  $\text{SrRuO}_3$  (002)-reflection peaks as measured for 85 nm-thick SRO films epitaxially grown on SAO (40 nm) in the as-deposited state (black curve, after step 1, Figure 1a), as well as after membrane transfer (after step 4, Figure 1d) using the flip-chip bonder (red curve) or manual method (blue curve).

remain nearly unchanged after transfer (within experimental errors), with  $3.935 \text{ \AA} \pm 0.005 \text{ \AA}$  for the out-of-plane and  $3.934 \text{ \AA} \pm 0.004 \text{ \AA}$  for in-plane lattice parameters.

Rocking-curves (RCs) of as-grown and transferred membranes produced in the same PLD process, but transferred either with use of the flip-chip bonder or via the manual process (see transfer method), are compared in Figure 4. The black curve corresponds to the as-grown sample (after step 1, Figure 1a); the red and blue curves refer to the transferred membranes (after step 4, Figure 1d) by means of the flip-chip bonder and the manual method, respectively. Clearly, the RCs of the as-grown films and transferred membranes are different, which indicates that the transfer process induces some structural defects by mechanical deformation. When using the flip-chip bonder, the FWHM of the RC peak increases only slightly from  $0.16^\circ$  to  $0.36^\circ$ . However, for the manual method, a much larger broadening of the FWHM up to  $0.84^\circ$  is observed. Rocking curve scans of the membranes were measured to analyze the distribution of domains which are not perfectly parallel. Defects like dislocations and curvatures create disruption in the parallelism of the atomic planes, resulting in a broadening of the RCs. To investigate the defect structures induced by the transfer process in more detail, the RCs were fitted with a pseudo-voigt peak function (as constructed from a linear combination of a Lorentzian and a Gaussian function, for more details see Supporting Information). If the single-crystal in-plane coherency is mainly affected by stacking faults due to misfit dislocations, its Fourier transform will approach a pure Lorentzian shape. If the domain disorder is caused by a spread of crystal plane orientations (mosaicity), the RC will approach a Gaussian distribution.<sup>[58–60]</sup> Peak shape analysis of the RCs in Figure 4 indicate that the Gaussian contribution to the RC is rather small for the as-grown films (about 10%), but its value is considerably increased after the transfer. While the Gaussian contribution is around 39% for the flip-chip bonder transfer, it

reaches 51% for the manual transfer method. The peak shape analysis thus suggests that the main type of defects introduced by the transfer procedure is mosaic defects, that is, crystal domains with different angular distributions. As concluded from the lower FWHM and lower Gaussian contribution of the measured RCs, the flip-chip bonder transfer method induces a significantly lower defect density. This should be expected, since the manual method provides a less accurate control of: i) the Ag bond-line thickness, ii) the parallel alignment of the bonding planes (i.e., as defined by the two Au-metallized surfaces), iii) the uniformity of the applied pressure gradient during sinter-bonding, and iv) the applied time–temperature profile during sinter-bonding. Consequently, the sinter-bonding step using the manual transfer method will typically induce higher thermo-mechanical stress gradients on the membrane during sinter-bonding, which may not only introduce structural defects during the sinter-bonding step, but also by a more irregular membrane relaxation during the SAO dissolution step.

## 2.4. Morphology of Transferred Membrane

A schematic representation of a successfully transferred STO/SRO bilayer membrane is shown in Figure 5a. For this specific example, a STO/SRO bilayer was grown and bonded manually using a  $50 \text{ }\mu\text{m}$  mask for stencil printing. Corresponding cross-sectional SEM micrographs images of the transferred membrane are shown in Figure 5b,c.

Here, the sintered Ag layer in the middle can be clearly identified by its characteristic porous structure. A lower porosity of the Ag bond zone can principally be achieved by application of higher bonding pressures, although this could be harmful for the relatively fragile oxide membranes. The top and bottom bonding interfaces appear flat and straight. At the bonding interfaces, the silver layer has reacted with the Au metallization layer upon sintering, forming an Au/Ag interdiffusion layer. Due to the complete miscibility of face-centered cubic (fcc) Ag and fcc Au,<sup>[61]</sup> a smooth, continuous transition between the Ag sinter layer and the Ag–Au interdiffusion layer is found. The interdiffusion between the sintering Ag nanoparticles and the Au metallization layer is driven by the negative enthalpy and Gibb's free energy of mixing in the system Ag–Au.<sup>[61]</sup> In the present example, a comparatively thick bilayer of STO( $\approx 180 \text{ nm}$ )/SRO( $\approx 180 \text{ nm}$ ) was used in order to better distinguish the transferred membrane from the Au/Ag metal in SEM. In fact, STO has a dark contrast, typical of an insulating material, while the metal layers of SRO and Au/Ag are brighter. No delamination between the original Au metallization layer and the membrane layers, or between the two membrane layers, can be observed. In particular, no buckling or bending of the membrane is observed, as frequently reported for other transfer methods.<sup>[41,48,62]</sup>

Figure 6 shows high-resolution SEM micrographs of a transferred membrane at different locations. No micro-scale defects such as cracks within the transferred layers or delaminations between the layers can be observed. At the immediate metal-oxide interface, a few dark imperfections are visible. These represent pores or contaminations that were probably introduced on the original STO-surface upon deposition of the

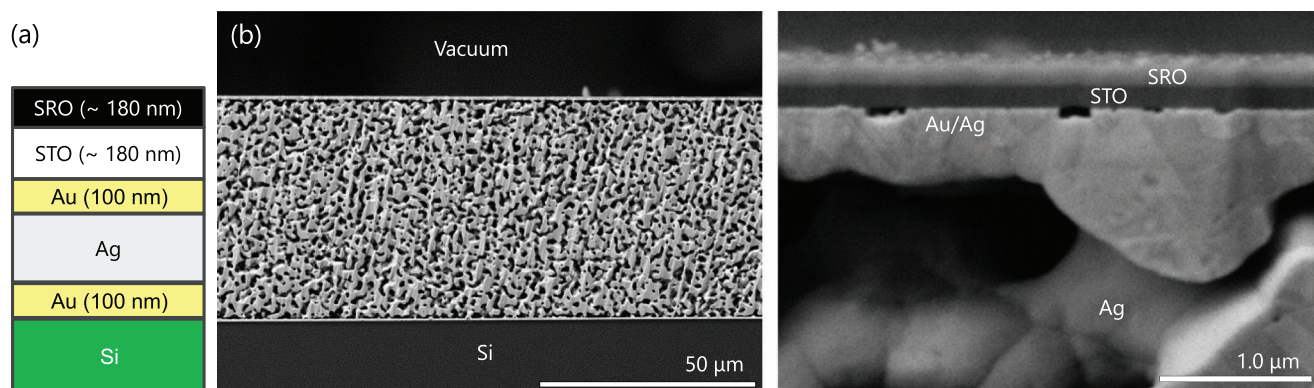


**Figure 5.** a) Schematic representation of a  $\text{SrRuO}_3$  ( $\approx 180$  nm)/ $\text{SrTiO}_3$  ( $\approx 180$  nm) membrane transferred by the manual method. The Au-coated Si host substrate has a surface area of  $3 \times 3$  mm<sup>2</sup>, while SRO film grown on parent substrate is  $5 \times 5$  mm<sup>2</sup> large. b) Cross-sectional SEM micrograph (recorded in back-scattered electron mode) of the transferred membrane at low magnification, c) zoom of the interface between the membrane and its bonding interface with the sintered Ag layer.

Au-metallization. The high integrity of the transferred membrane after the Ag sinter-bonding process can be attributed to a combination of several factors:

- The sintering of the Ag nanoparticles (to each other and to the Au metallization layers) is a comparatively slow process without rapid volume changes (e.g., compared to solidification processes, as in the case of soldering).
- Bond formation between the Ag nanopaste and the Au-metallization of the membrane is realized by formation of an Ag–Au transition layer via solid-state interdiffusion; this mitigates the influence of the nanopaste bonding process (i.e., of paste decomposition and Ag nanoparticle sintering) on the oxide membrane.
- A firm mechanical support of the membrane is maintained during the entire membrane transfer process.

Figure 7a,b shows light optical micrographs and corresponding line profilometer measurements of 85-nm-thick SRO membranes transferred by the flip-chip bonder and manual method, respectively (using a stencil printing mask of  $4 \times 4$  mm<sup>2</sup>). The edges of the transferred membrane are irregularly fractured along the edges of the Ag/Au layer during the dissolution step (cf. orange ellipse in Figure 7b, labeled

“delamination”). The Au metallization on the host substrate is clearly distinguishable. A higher percentage of transferred membrane (in principle up to 100%) with more regular edges could be obtained by optimizing the mask size for stencil printing with respect to the original membrane size. The bonding area of the membrane (except for its edges) is very flat without any delamination or cracks. Notably, membrane transfer with the manual method results in a considerable larger misalignment of the membrane surface with respect to that of the host substrate: the respective misalignment angles are  $0.07^\circ \pm 0.01^\circ$  and  $0.37^\circ \pm 0.01^\circ$  for the flip-chip bonder and manual transfers pertaining to Figure 7a,b, respectively. As discussed in Section 4, the manual transfer method does not allow a precise control of the Ag bond-line thickness, the parallel alignment of the bonding planes and the uniformity of the applied pressure gradient during sinter-bonding. It resulted in a small paste overflow that was scratched (left of the micrograph on Figure 7b) to properly separate the membrane from the parent substrate. Hence, the flip-chip bonder method results in a much better membrane quality both with respect to mechanical deformation (see Section 4) and in-plane parallelism.

Figure 8a,b shows 3D image reconstructions of a SRO membrane (thickness  $\approx 85$  nm;  $4 \times 4$  mm<sup>2</sup>) transferred by the

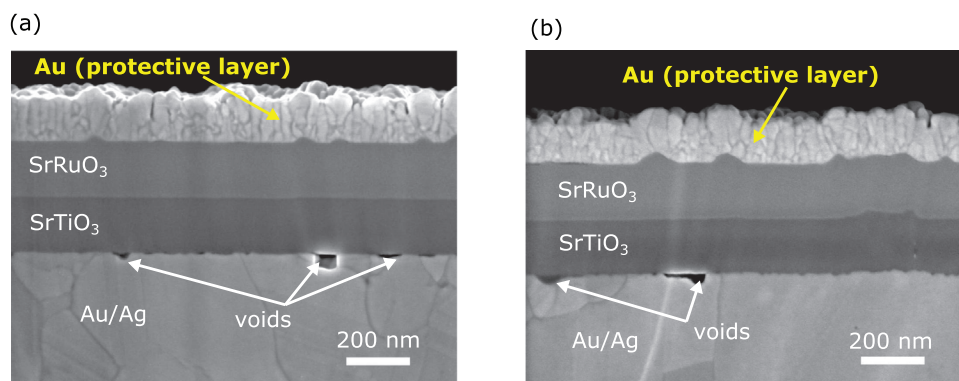


**Figure 6.** Cross-sectional high-resolution SEM (immersion lens detector) micrograph of a transferred membrane as reported in Figure 5. a,b) Two representative regions of the cross-section both in a field of view (horizontal) of  $1.4 \mu\text{m}$ . Some voids or inclusions are visible along the metal-oxide interface, which probably result from the metallization process.

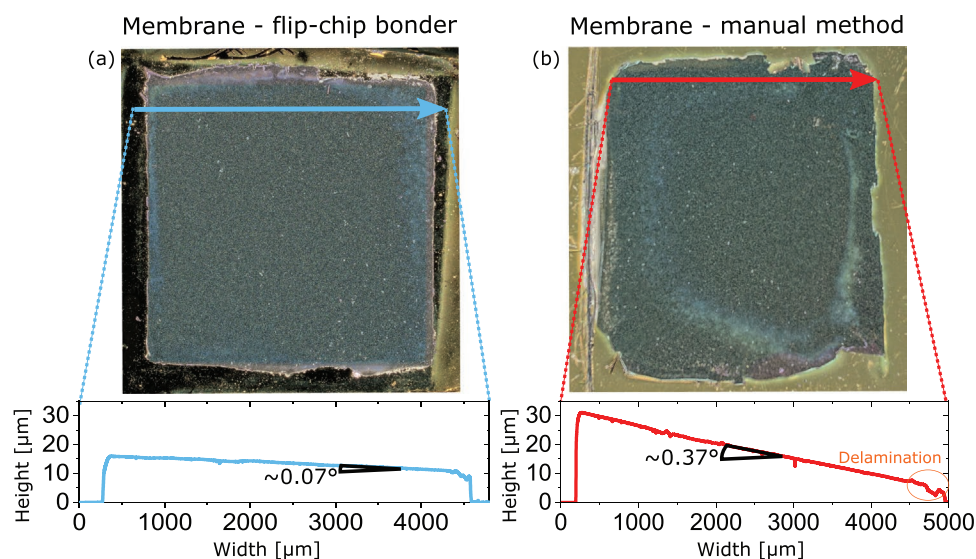


**Figure 7.** (Top) Optical microscope images of two  $\text{SrRuO}_3$  ( $\approx 85$  nm) membranes. (Bottom) Corresponding profilometer measurements. a) Membrane fabricated with the flip-chip bonder. b) Membrane fabricated with the “manual method.” For both transfer methods: before transfer, SAO thickness was 40 nm, original films surface was  $5 \times 5 \text{ mm}^2$  and mask size for stencil printing was  $4 \times 4 \text{ mm}^2$  with a thickness of 20  $\mu\text{m}$ .

flip-chip-bonder method on a Si host substrate (thickness 500  $\mu\text{m}$ ;  $5 \times 5 \text{ mm}^2$ ) using a  $4 \times 4 \text{ mm}^2$  mask for Ag stencil printing. The 3D reconstructions were obtained by acquiring 2D images at different heights using light optical microscopy.

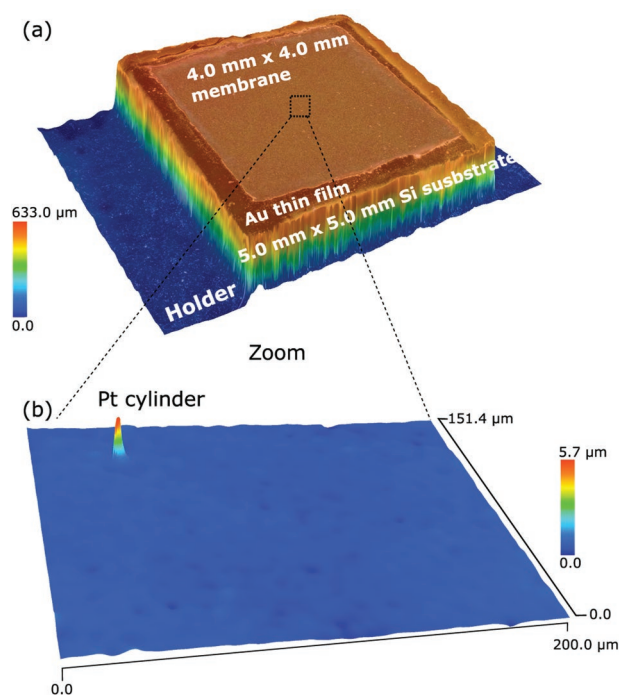


**Figure 8.** a) 3D microscope image reconstruction of a transferred  $\text{SrRuO}_3$  membrane (thickness  $\approx 85$  nm;  $4 \times 4 \text{ mm}^2$ ) on a Si host substrate (thickness 500  $\mu\text{m}$ ;  $5 \times 5 \text{ mm}^2$ ). The mask area for Ag stencil printing was  $4 \times 4 \text{ mm}^2$  with a bond line thickness of 20  $\mu\text{m}$ . The membrane is transferred using the flip-chip bonder. b) 3D microscope image reconstruction at higher magnification of a central area on the membrane surface. A Pt pillar ( $\approx 3 \mu\text{m}$  diameter and  $\approx 6 \mu\text{m}$  height) was deposited on purpose to calibrate the height scale of the instrument.

In the low-magnification image of Figure 8a, the membrane appears totally flat with respect to the substrate surface plane. In order to resolve smaller variations of the surface topology, several 3D images were acquired with a smaller field of view ( $\approx 400 \mu\text{m} \times 500 \mu\text{m}$ ) at randomly selected positions on the membrane surface. The height variations were always smaller than  $\pm 0.5 \mu\text{m}$ . In a selected region, a Pt cylinder of 3  $\mu\text{m}$  in diameter and 4.5  $\mu\text{m}$  in height was deposited using a Ga-focused ion beam (FIB) system to verify the microscope’s ability to image structures with a z-height close to the resolution limit of  $\Delta z \approx 0.5 \mu\text{m}$ . Indeed, the tiny cylinder is clearly visible in Figure 8b and it represents a scale bar which authorizes us to conclude that all the observed regions of the membrane are flat within our optical resolution ( $\approx 0.5 \mu\text{m}$ ).

Figure 9 shows an AFM image of a transferred membrane (thickness 20 nm;  $4 \times 4 \text{ mm}^2$ ) using the flip-chip bonder. As the original SRO/SAO interface becomes the top surface after the dissolution of the SAO sacrificial layer, the quality of this surface is expected to be correlated to the SAO thickness. Indeed, a root mean square (RMS) roughness of less than 1 nm is measured on a surface area of  $2.0 \mu\text{m} \times 2.0 \mu\text{m}$ . Any small protrusions on the membrane surface are likely residuals from water or dust particles.

Hence, it may be concluded that the transferred membrane is extremely flat over the entire bonded area of  $4 \times 4 \text{ mm}^2$ . With the proposed transfer method, very low roughness values over extended membrane areas are achieved, which allows micro-nano-processing, that is, the building oxide membrane devices.

### 3. Conclusion

In this study, a novel procedure for functional oxide membrane fabrication and transfer is presented. Advantages of sacrificial (water-soluble) SAO interlayers are combined with the



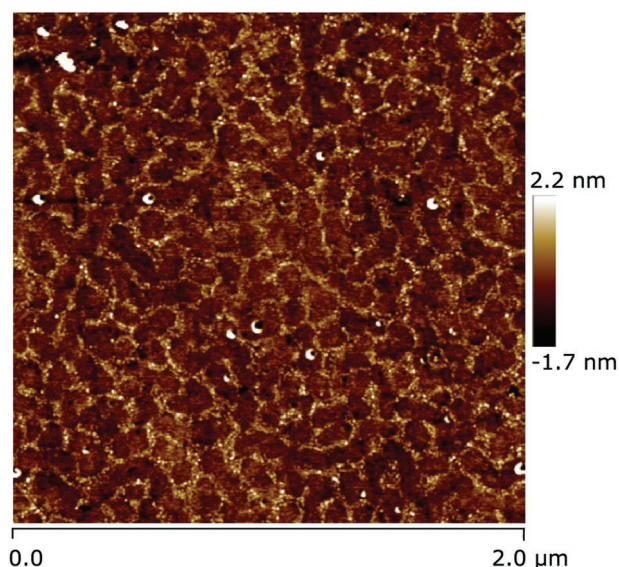


**Figure 9.** AFM micrograph of a  $\approx 20$  nm-thick  $\text{SrRuO}_3$  membrane transferred by the flip-chip bonder method. The final membrane area is about  $4 \times 4 \text{ mm}^2$  (cf. Figure 8). Here, an AFM scan over a selected region of  $2 \times 2 \mu\text{m}^2$  is reported. The SRO/SAO interface becomes the top surface of the membrane after the dissolution of the sacrificial layer. Therefore, the roughness of this surface is expected to correlate with the SAO thickness (here  $\approx 20$  nm-thick). A root mean square (RMS) roughness of  $0.63 \pm 0.04$  nm was calculated from the z-scan.

advantages of a low-temperature Ag nanopaste sinter-bonding process. The Ag sinter-bonding process creates a very strong and rigid metallic bond between membrane and host substrate. The use of a flip-chip bonder instrument for the sinter-bonding step provides improved control of the Ag bond-line thickness, the parallel alignment of the bonding planes, the uniformity of the applied pressure gradient and the applied time-temperature profile. As such, the as-grown structure and properties of the transferred membrane are largely preserved. By using the proposed procedure, the membranes show no cracks and no plastic deformations. Membrane delamination is found to be limited to the edges of the sinter-bonded area. The transferred membranes are smooth, and a extremely low surface roughness is observed over large areas. The surface morphology of the transferred membranes is characterized by AFM, which shows a roughness of the top layer of the transferred membrane of less than 1 nm. Cross-sectional analyses by LOM and SEM evidence a straight interface and very smooth membrane surface, which is crack- and wrinkle-free across the entire sinter-bonded area (except for the outer edges). The thus obtained membrane properties seems to be suitable for building oxide membrane devices.

The method proposed thus paves the way toward an improved technology for oxide membrane transfer that is practical and reproducible, and also produces a solid and firm bond to the host substrate. In the future, one could consider to introduce intermediate layers, like for instance Ni, Ti, TiW,  $\text{TiO}_2$ ,  $\text{SrTiO}_3$ , etc. on top of the functional oxides or on top of the Si host substrate, to ensure an even stronger adhesion of the membrane to the host substrate for surviving externally applied strains upon mechanical straining for example, upon bending.

To implement our method in standard electronics, further development will be needed to reduce the thickness of the solid metallic layer. This will allow for standard process like for instance typical wet and dry etching.

The proposed membrane transfer procedure will contribute to the development of membrane-based devices in the years to come, as it presents many advantages compared to the hitherto applied procedures for oxide membrane transfer.

## 4. Experimental Section

**Substrate Preparation:** (001)-oriented STO substrates were treated following the standard procedure in ref. [63] to obtain a  $\text{TiO}_2$ -termination. After the chemical etching, they were first cleaned for 5 min in ultrasonic bath with successive solvents (acetone, ethanol, isopropanol, milliQ-water, and isopropanol) and dried with an  $\text{N}_2$  gun. Afterward, they were annealed in a furnace with continuous  $\text{O}_2$  flow, with a heating ramp of  $5^\circ\text{C min}^{-1}$ , a dwell time of 8 h at  $950^\circ\text{C}$ , and cool down with  $5^\circ\text{C min}^{-1}$  till below  $300^\circ\text{C}$ , at which point the  $\text{O}_2$  flow was stopped.

**Pulsed Laser Deposition:** The STO substrates were mounted with conductive silver glue onto a holder which could be heated to very high temperature. The laser was a Nd:YAG with a 266 nm wavelength from Q-smart (850 mJ) laser with harmonic modules). Temperature was measured with a thermocouple directly in contact with the samples, which ensured a very precise measurement. The working distance was 45 mm. Materials were grown at  $725^\circ\text{C}$  for STO and SRO and  $800^\circ\text{C}$  for SAO. The internal pulse energy of the laser was  $\approx 40$  mJ with a rate of 2 Hz and a spot size diameter of  $\approx 1.2$  mm. Best quality of SAO was grown in vacuum ( $10^{-5}$  mbar), while STO and SRO were grown with  $\text{O}_2$  partial pressures of 10 and 100 mTorr, respectively.

**Bonding Procedure:** On top of the initial and host substrates Au deposition (100 nm) was performed with a Leica sputter coater ACE200. Deposition was performed with a sputter mask on the as-grown film part in order to protect the edge of the SAO thin film from Au deposition. Then, an Ag nanopaste (NanoTach-X from NBETech, LLC) was applied on one or the other surface by stencil printing with a  $20 \mu\text{m}$ -thick foil of stainless steel. Edge protection during the entire bonding procedure was crucial in order to enable membrane release. For performing the bonding process by nanopaste sintering, a manual flip-chip bonder (Fineplacer Pico ma from Finetech, Berlin, Germany) was employed, which allowed to control the parallelism between the initial and host substrate during bonding, and to apply defined bonding pressures and time-temperature programs. For the sintering procedure, annealing was performed with a ramp of  $5\text{--}7^\circ\text{C min}^{-1}$ , a dwell time of 30 min at around  $250^\circ\text{C}$ , and an applied bonding force of around 2 N. In an alternative procedure ("manual method"), instead of using the flip-chip bonder, samples were assembled manually and placed into an air furnace with a weight of  $\approx 200$  g ( $\approx 2$  N) on top of the sample and heated in a temperature range between 250 and  $260^\circ\text{C}$  for 30 min with here also a ramp of  $5\text{--}7^\circ\text{C min}^{-1}$ . Cooling down was just performed by switching off the furnace in this second method.

**Dissolution Procedure:** After the bonding procedure, the sample was immersed in milliQ-water. Partial separation with STO substrate could be achieved within 1 day or even less. However, to ensure total dissolution of SAO layers, samples were left 4 days in milliQ-water before the membrane was released. After release, the membrane on top of the Si substrate was dried around 1 h in air or with a  $\text{N}_2$  gun.

**Membrane Characterization:** As-grown films and membranes quality was assessed with an AFM Bruker ICON 3 in order to evaluate the surface state and roughness. X-ray diffraction (XRD) scans were carried out with a Bruker Discovery 8 diffractometer in order to study the phase, the orientation, stress relations, and coherency between the different crystalline structures of the stacks. With the same equipment, X-ray reflectivity (XRR) was also performed in order to determine the thickness of the layers.

A stereo microscope Leica M205 C, a Nikon Microphot-FXA, and a KEYENCE VHX-7000 microscope were used to evaluate the surface



morphology. For the investigation of the microstructure after bonding, cross-sections were prepared by ion milling (Hitachi IM4000). The cross-sections were analyzed with SEM-EDS using a Hitachi S3700N equipped with an Octane Pro EDS detector (EDAX/Ametek). For high-resolution SEM (HR-SEM) cross-sectional analysis, the surfaces of the transferred membranes were additionally coated by a protective Au layer before ion milling. HR-SEM analysis was performed using a Zeiss Gemini SEM 460 with an inlense secondary electron detector.

Profilometry was performed with a Bruker Dektak XT 2D profilometer. X-ray photospectrometry (XPS) was performed before and after membrane transfer using a QUANTES, physical electronic system, with Al K $\alpha$  radiation (1486.7 eV) using a pass energy of 280 eV for survey spectra and of 69 eV for core level acquisitions in order to quantify SAO residues after transfer.

**Statistical Analysis:** Fitting procedure in this article had been performed by OriginLab software. For all the calculations in this article standard method for error propagation had been always implemented. All standard error  $\sigma$  (confident band of  $\approx 66\%$ ), obtained by the fitting procedure, had been converted to absolute errors ( $\approx 3 \times \sigma$ , confident band of  $\approx 99\%$ ) before to be presented with the corresponding quantity.

XRR and AFM data had been analyzed by means of instrumental software Leptos7 (Bruker) and NanoScope Analysis (Bruker), respectively.

## Supporting Information

Supporting Information is available from the Wiley Online Library or from the author.

## Acknowledgements

The authors gratefully acknowledge internal funding from Empa (Internal Research Call 2020, SOXMEM 5213.00204). Authors would like to acknowledge Jonas Gartmann (Empa) for his help in designing several tools that were needed for this project, Tobias Burgdorf (Empa) for his collaboration during some experiments and Anaïs Gozzi for her help in the design of Figure 1.

Open access funding provided by ETH-Bereich Forschungsanstalten.

## Conflict of Interest

The authors declare no conflict of interest.

## Data Availability Statement

The data that support the findings of this study are available from the corresponding author upon reasonable request.

## Keywords

epitaxial films, flexible electronics, functional oxides, membranes, perovskite oxides

Received: July 3, 2022

Revised: August 22, 2022

Published online: September 30, 2022

[1] D. W. Bruce, D. O'Hare, R. I. Walton, in *Functional Oxides*, Vol. 12, John Wiley & Sons, Hoboken, NJ **2011**, Ch. 1.

[2] M. Coll, J. Fontcuberta, M. Althammer, M. Bibes, H. Boschker, A. Calleja, G. Cheng, M. Cuoco, R. Dittmann, B. Dkhil, I. El Baggari,

M. Fanciulli, I. Fina, E. Fortunato, C. Frontera, S. Fujita, V. Garcia, S. T. B. Goennenwein, C. G. Granqvist, J. Grollier, R. Gross, A. Hagfeldt, G. Herranz, K. Hono, E. Houwman, M. Huijben, A. Kalaboukhov, D. J. Keeble, G. Koster, L. F. Kourkoutis, et al., *Appl. Surf. Sci.* **2019**, 482, 1.

[3] G. Koster, M. Huijben, G. Rijnders, *Epitaxial Growth of Complex Metal Oxides*, Elsevier, Amsterdam, Netherlands **2015**.

[4] R. A. McKee, F. Walker, M. Chisholm, *Phys. Rev. Lett.* **1998**, 81, 3014.

[5] S. Sakai, R. Ilangoan, *IEEE Electron Device Lett.* **2004**, 25, 369.

[6] K. Takahashi, K. Aizawa, B.-E. Park, H. Ishiwara, *Jpn. J. Appl. Phys.* **2005**, 44, 6218.

[7] W. C. Goh, K. Yao, C. Ong, *J. Appl. Phys.* **2005**, 97, 073905.

[8] R. J. Baker, *CMOS: Circuit Design, Layout, and Simulation*, John Wiley & Sons, Hoboken, NJ **2019**, Ch. 7.2.2.

[9] D. Lehninger, R. Olivo, T. Ali, M. Lederer, T. Kämpfe, C. Mart, K. Biedermann, K. Kühnel, L. Roy, M. Kalkani, K. Seidel, *Phys. Status Solidi A* **2020**, 217, 1900840.

[10] T. Francois, L. Grenouillet, J. Coignus, P. Blaise, C. Carabasse, N. Vaxelaire, T. Magis, F. Aussenac, V. Loup, C. Pellissier, S. Slesazek, V. Havel, C. Richter, A. Makosiej, B. Giraud, E. T. Breyer, M. Materano, P. Chiquet, M. Bocquet, E. Nowak, U. Schroeder, F. Gaillard, in *2019 IEEE Int. Electron Devices Meeting (IEDM)*, IEEE, Piscataway, NJ **2019**, pp. 15–7.

[11] E. Yablonovitch, T. Gmitter, J. Harbison, R. Bhat, *Appl. Phys. Lett.* **1987**, 51, 2222.

[12] H. Kum, D. Lee, W. Kong, H. Kim, Y. Park, Y. Kim, Y. Baek, S.-H. Bae, K. Lee, J. Kim, *Nat. Electron.* **2019**, 2, 439.

[13] S. R. Bakaul, C. R. Serrao, M. Lee, C. W. Yeung, A. Sarker, S.-L. Hsu, A. K. Yadav, L. Dedon, L. You, A. I. Khan, J. D. Clarkson, C. Hu, R. Ramesh, S. Salahuddin, *Nat. Commun.* **2016**, 7, 10547.

[14] Q. Gan, R. Rao, C. Eom, J. Garrett, M. Lee, *Appl. Phys. Lett.* **1998**, 72, 978.

[15] D. M. Paskiewicz, R. Sichel-Tissot, E. Karapetrova, L. Stan, D. D. Fong, *Nano Lett.* **2016**, 16, 534.

[16] L. Tsakalakos, T. Sands, *Appl. Phys. Lett.* **2000**, 76, 227.

[17] I. Szafraniak, I. Radu, R. Scholz, M. Alexe, U. Gösele, *Integr. Ferroelectr.* **2003**, 55, 983.

[18] D. Lu, D. J. Baek, S. S. Hong, L. F. Kourkoutis, Y. Hikita, H. Y. Hwang, *Nat. Mater.* **2016**, 15, 1255.

[19] Z. Zhao, A. Abdelsamie, R. Guo, S. Shi, J. Zhao, W. Lin, K. Sun, J. Wang, J. Wang, X. Yan, J. Chen, *Nano Res.* **2021**, 15, 2682.

[20] Z. Lu, Y. Yang, L. Wen, J. Feng, B. Lao, X. Zheng, S. Li, K. Zhao, B. Cao, Z. Ren, D. Song, H. Du, Y. Guo, Z. Zhong, X. Hao, Z. Wang, R. W. Li, *npj Flexible Electron.* **2022**, 6, 9.

[21] S. S. Hong, J. H. Yu, D. Lu, A. F. Marshall, Y. Hikita, Y. Cui, H. Y. Hwang, *Sci. Adv.* **2017**, 3, eaao5173.

[22] D. Ji, S. Cai, T. R. Paudel, H. Sun, C. Zhang, L. Han, Y. Wei, Y. Zang, M. Gu, Y. Zhang, W. Gao, H. Huan, W. Guo, D. Wu, Z. Gu, E. Y. Tsybal, P. Wang, Y. Nie, X. Pan, *Nature* **2019**, 570, 87.

[23] M. Lee, M. P. Robin, R. H. Guis, U. Filippozzi, D. H. Shin, T. C. Van Thiel, S. P. Paardekooper, J. R. Renshof, H. S. Van Der Zant, A. D. Caviglia, G. J. Verbiest, P. G. Steeneken, *Nano Lett.* **2022**, 22, 1475.

[24] Z.-D. Luo, M.-M. Yang, M. Alexe, *ACS Appl. Electron. Mater.* **2019**, 2, 310.

[25] Z. Chen, B. Y. Wang, B. H. Goodge, D. Lu, S. S. Hong, D. Li, L. F. Kourkoutis, Y. Hikita, H. Y. Hwang, *Phys. Rev. Mater.* **2019**, 3, 060801.

[26] S. S. Hong, M. Gu, M. Verma, V. Harbola, B. Y. Wang, D. Lu, A. Vailonis, Y. Hikita, R. Pentcheva, J. M. Rondinelli, H. Y. Hwang, *Science* **2020**, 368, 71.

[27] J. Park, J. H. Shin, K. Song, Y.-J. Kim, H.-B. Jang, H. Lee, H.-S. Sim, C.-H. Yang, *Appl. Phys. Lett.* **2020**, 116, 022401.

[28] R. Xu, J. Huang, E. S. Barnard, S. S. Hong, P. Singh, E. K. Wong, T. Jansen, V. Harbola, J. Xiao, B. Y. Wang, S. Crossley, D. Lu, S. Liu, H. Y. Hwang, *Nat. Commun.* **2020**, 11, 3141.

- [29] H. Sun, C. Zhang, J. Song, J. Gu, T. Zhang, Y. Zang, Y. Li, Z. Gu, P. Wang, Y. Nie, *Thin Solid Films* **2020**, 697, 137815.
- [30] P. Salles, I. Caño, R. Guzman, C. Dore, A. Mihi, W. Zhou, M. Coll, *Adv. Mater. Interfaces* **2021**, 8, 2001643.
- [31] Z. Xie, Z. Li, H. Lu, Y. Wang, Y. Liu, *Ceram. Int.* **2021**, 47, 13528.
- [32] P. T. Le, E. Johan, G. Koster, *Sci. Rep.* **2021**, 11, 12435.
- [33] Z.-D. Luo, J. J. Peters, A. M. Sanchez, M. Alexe, *ACS Appl. Mater. Interfaces* **2019**, 11, 23313.
- [34] Z. Lu, J. Liu, J. Feng, X. Zheng, L.-h. Yang, C. Ge, K.-j. Jin, Z. Wang, R.-W. Li, *APL Mater.* **2020**, 8, 051105.
- [35] F. An, K. Qu, G. Zhong, Y. Dong, W. Ming, M. Zi, Z. Liu, Y. Wang, B. Qi, Z. Ding, J. Xu, Z. Luo, X. Gao, S. Xie, P. Gao, J. Li, *Adv. Funct. Mater.* **2020**, 30, 2003495.
- [36] B. Zhang, C. Yun, J. L. MacManus-Driscoll, *Nano-Micro Lett.* **2021**, 13, 39.
- [37] K. Han, L. Wu, Y. Cao, H. Wang, C. Ye, K. Huang, M. Motapothula, H. Xing, X. Li, D.-C. Qi, X. Li, X. R. Wang, *ACS Appl. Mater. Interfaces* **2021**, 13, 16688.
- [38] Q. Jin, H. Cheng, Z. Wang, Q. Zhang, S. Lin, M. A. Roldan, J. Zhao, J.-O. Wang, S. Chen, M. He, C. Ge, C. Wang, H.-B. Lu, H. Guo, L. Gu, X. Tong, T. Zhu, S. Wang, H. Yang, K.-J. Jin, E.-J. Guo, *Adv. Mater.* **2021**, 33, 2005920.
- [39] C. Jin, Y. Zhu, X. Li, F. An, W. Han, Q. Liu, S. Hu, Y. Ji, Z. Xu, S. Hu, M. Ye, G. Zhong, M. Gu, L. Chen, *Adv. Sci.* **2021**, 8, 2102178.
- [40] Y. Zang, C. Di, Z. Geng, X. Yan, D. Ji, N. Zheng, X. Jiang, H. Fu, J. Wang, W. Guo, H. Sun, L. Han, Y. Zhou, Z. Gu, D. Kong, H. Aramberri, C. Cazorla, J. Íñiguez, R. Rurali, L. Chen, J. Zhou, D. Wu, M. Lu, Y. Nie, Y. Chen, X. Pan, *Adv. Mater.* **2022**, 34, 2105778.
- [41] K. Gu, T. Katayama, S. Yasui, A. Chikamatsu, S. Yasuhara, M. Itoh, T. Hasegawa, *Adv. Funct. Mater.* **2020**, 30, 2001236.
- [42] A. Sambri, M. Scuderi, A. Guarino, E. D. Gennaro, R. Erlandsen, R. T. Dahm, A. V. Bjørlig, D. V. Christensen, R. D. Capua, B. D. Ventura, U. Scotti di Uccio, S. Mirabella, G. Nicotra, C. Spinella, T. S. Jespersen, F. M. Granozio, *Adv. Funct. Mater.* **2020**, 30, 1909964.
- [43] V. Shautsova, A. M. Gilbertson, N. C. Black, S. A. Maier, L. F. Cohen, *Sci. Rep.* **2016**, 6, 30210.
- [44] M. J. Allen, V. C. Tung, L. Gomez, Z. Xu, L.-M. Chen, K. S. Nelson, C. Zhou, R. B. Kaner, Y. Yang, *Adv. Mater.* **2009**, 21, 2098.
- [45] X.-D. Chen, Z.-B. Liu, C.-Y. Zheng, F. Xing, X.-Q. Yan, Y. Chen, J.-G. Tian, *Carbon* **2013**, 56, 271.
- [46] D. G. Papageorgiou, I. A. Kinloch, R. J. Young, *Prog. Mater. Sci.* **2017**, 90, 75.
- [47] Q. Wang, H. Fang, D. Wang, J. Wang, N. Zhang, B. He, W. Lü, *Crystals* **2020**, 10, 733.
- [48] G. Dong, S. Li, T. Li, H. Wu, T. Nan, X. Wang, H. Liu, Y. Cheng, Y. Zhou, W. Qu, Y. Zhao, B. Peng, Z. Wang, Z. Hu, Z. Luo, W. Ren, S. J. Pennycook, J. Li, J. Sun, Z.-G. Ye, Z. Jiang, Z. Zhou, X. Ding, T. Min, M. Liu, *Adv. Mater.* **2020**, 32, 2004477.
- [49] G. Koster, L. Klein, W. Siemons, G. Rijnders, J. S. Dodge, C.-B. Eom, D. H. Blank, M. R. Beasley, *Rev. Mod. Phys.* **2012**, 84, 253.
- [50] C.-Z. Hu, Y.-S. Zhang, X. Niu, N. Zhong, P.-H. Xiang, C.-G. Duan, *Appl. Phys. Lett.* **2021**, 118, 072407.
- [51] K. S. Siow, *J. Alloys Compd.* **2012**, 514, 6.
- [52] D. Li, C. Adamo, B. Y. Wang, H. Yoon, Z. Chen, S. S. Hong, D. Lu, Y. Cui, Y. Hikita, H. Y. Hwang, *Nano Lett.* **2021**, 21, 4454.
- [53] D. J. Baek, D. Lu, Y. Hikita, H. Y. Hwang, L. F. Kourkoutis, *APL Mater.* **2017**, 5, 096108.
- [54] B. C. Chakoumakos, G. A. Lager, J. A. Fernandez-Baca, *Acta Crystallogr., Sect. C: Struct. Chem.* **1992**, 48, 414.
- [55] Sr<sub>3</sub>Al<sub>2</sub>O<sub>6</sub> crystal structure: Datasheet from “pauling file multinaries edition – 2012” in Springer Materials, [https://materials.springer.com/isp/crystallographic/docs/sd\\_0376471](https://materials.springer.com/isp/crystallographic/docs/sd_0376471) (accessed: 2016).
- [56] H. Yao, K. Jin, Z. Yang, Q. Zhang, W. Ren, S. Xu, M. Yang, L. Gu, E.-J. Guo, C. Ge, C. Wang, X. Xu, D. Zhang, G. Yang, *Adv. Mater. Interfaces* **2021**, 8, 2101499.
- [57] H. Samata, Y. Saeki, S. Mizusaki, Y. Nagata, T. Ozawa, A. Sato, *J. Cryst. Growth* **2009**, 311, 623.
- [58] P. F. Fewster, *Rep. Prog. Phys.* **1996**, 59, 1339.
- [59] V. Holý, J. Kuběna, E. Abramof, K. Lischka, A. Pesek, E. Koppensteiner, *J. Appl. Phys.* **1993**, 74, 1736.
- [60] V. Kaganer, R. Köhler, M. Schmidbauer, R. Opitz, B. Jenichen, *Phys. Rev. B* **1997**, 55, 1793.
- [61] H. Okamoto, T. B. Massalski, *Bull. Alloy Phase Diagrams* **1983**, 4, 30.
- [62] H. Nishikawa, S. Umatani, T. Mizuyama, A. Hiraoka, K. Mikami, *Sensors* **2021**, 21, 7326.
- [63] T. Gagnidze, H. Ma, C. Cancellieri, G.-L. Bona, F. La Mattina, *Sci. Technol. Adv. Mater.* **2019**, 20, 456.